Spatio-temporal evolution of hydroxyapatite crystal thickness at the bone-implant interface

Sophie Le Cann, Elin Törnquist, Isabella Silva Barreto, Manon Fraulob, Hugues Albini Lomami, Mariana Verezhak, Manuel Guizar-Sicairos, Hanna Isaksson, Guillaume Haiat

Spatio-temporal evolution of hydroxyapatite crystal thickness at the bone-implant interface

Sophie Le Cann[1*], Elin Törnquist[2], Isabella Silva Barreto[2], Manon Fraulob[1], Hugues Albini Lomami[1], Mariana Verezhak[3], Manuel Guizar-Sicairos[3], Hanna Isaksson[2], Guillaume Haïat[1]

[1] *CNRS, Univ Paris Est Creteil, MSME UMR 8208, F-94010 Creteil, France*

[2] *Department of Biomedical Engineering, Lund University, 221 00 Lund, Sweden*

[3] *Paul Scherrer Institut, Forschungsstrasse 111, Villigen 5232, Switzerland*

* CORRESPONDING AUTHOR:

Sophie Le Cann

Laboratoire Modélisation et Simulation Multi Echelle (MSME), Equipe Biomécanique

Université Paris-Est Créteil Val de Marne (UPEC), Faculté des Sciences et Technologie

61, Avenue du Général de Gaulle 94010 Créteil Cedex - FRANCE

E-mail: sophie.le-cann@u-pec.fr

KEYWORDS: Bone-implant interface, small-angle x-ray scattering, osseointegration, hydroxyapatite

Abstract

A better understanding of bone nanostructure around the bone-implant interface is essential to improve longevity of clinical implants and decrease failure risks. This study investigates the spatio-temporal evolution of mineral crystal thickness and plate orientation in newly formed bone around the surface of a metallic implant. Standardized coin-shaped titanium implants designed with a bone chamber were inserted into rabbit tibiae for 7 and 13 weeks. Scanning measurements with micro-focused small-angle X-ray scattering (SAXS) were carried out on newly formed bone close to the implant and in control mature cortical bone. Mineral crystals were thinner close to the implant (1.8 ± 0.45 nm at 7 weeks and 2.4 ± 0.57 nm at 13 weeks) than in the control mature bone tissue (2.5 ± 0.21 nm at 7 weeks and 2.8 ± 0.35 nm at 13 weeks), with increasing thickness over healing time (+30 % in 6 weeks). These results are explained by younger bone close to the implant, which matures during osseointegration. Thinner mineral crystals parallel to the implant surface within the first 100 µm close to the implant indicate that the implant affects bone ultrastructure close to the implant, potentially due to heterogeneous interfacial stresses, and suggest a longer maturation process of bone tissue and difficulty in binding to the metal. The bone growth kinetics within the bone chamber was derived from the spatio-temporal evolution of bone tissue's nanostructure, coupled with microtomographic imaging. The findings indicate that understanding mineral crystal thickness or plate orientation can improve our knowledge of osseointegration.

1. Introduction

Osseointegration of metallic implants is key for the long-term survival of dental and orthopaedic prostheses. Bone ingrowth onto and around a metallic foreign body occurs over time and creates a bone-implant interface. Early implant failure (within the first 6 months after implantation) is linked to an inability to establish intimate bone-implant contact, and is a common cause of failures in implant dentistry [1,2]. The reasons behind osseointegration failure are complex to isolate, and could rise from multiple factors related to the implant, the surgical procedure and the patient [3,4]. To improve implant stability, a better understanding of the biomechanical properties of the bone-implant interface and the surrounding bone tissues are required [5,6]. Bone's unique hierarchical structure, the combined effect of its chemical, structural and mechanical properties, as well as the temporal evolution of new tissue formation during osseointegration, require the use of a large variety of approaches to investigate the bone-implant interface, from the macro down to the nanoscale [7]. Clinically relevant implants, such as dental implants or pedicle screws, have been widely studied [8] but remain of limited interest for understanding osseointegration phenomena as such implants do not allow to work under reproducible and standardized mechanical conditions. Instead, models such as bone chambers and/or flat surfaces-implants have been developed [9–11]. The bone-implant construct has been widely investigated at the macro- and micro-scales, to e.g. clarify the effect of implant design [12] and bone microstructure [6,13] on implant stability. The nanoscale has been overlooked for a long time, although our understanding of how bone composition, structure and mechanical properties are inter-linked has rapidly expanded thanks to high resolution tomographic, spectroscopic and microscopic techniques [14–17].

At the nanoscale, bone tissue is composed of an organic matrix (mostly collagen type I) and inorganic mineral crystals in forms of hydroxyapatite ($Ca_5(PO_4)_3OH$) [18]. The hydroxyapatite (HA) crystals are slightly curved platelets localized in gaps between collagen molecules, with their c-axes (long axes) aligned with the mineralized collagen fibrils [19,20]. To ultimately understand why and how an implant may loosen and fail, it is important to investigate the formation of the bone-implant interface and especially the adaptation of bone ultrastructure around an implant [21]. X-ray based scattering techniques, such as small-angle X-ray scattering (SAXS), are sensitive to the crystal structure and periodic arrangement of bone minerals, and can be used to retrieve information about mineral platelet orientation and thickness [22–26]. Mineral crystal thickness is closely linked to the variation in crystal volume [23] and relevant as it has been shown to increase during bone healing, when woven bone remodels into lamellar and/or cortical bone [24,26,27]. Moreover, bone ultrastructure orientation and arrangement are predictors of mechanical properties such as bone strength or elastic modulus [28]. Besides, a relationship between mineral crystal thickness and elastic properties of bone tissue has been observed [29,30]. Together, this motivates the investigation of how crystal thicknesses evolve and are arranged close to an implant, in order to understand the biomechanical properties of the bone-implant interface. Earlier studies have shown that peri-implant bone nanostructure is affected by the presence of ceramic and metallic implants [16,31] and evolves close to resorbable materials during degradation [27,32–34]. However, the spatial evolution of crystal thicknesses in newly formed bone at the interface remains unclear.

This study aims to evaluate the spatio-temporal evolution of hydroxyapatite crystal thickness and plate orientation within newly formed bone at a Titanium surface and to better understand the bone growth kinetics inside a standardized bone chamber model. A micro-focused small angle X-ray scattering (SAXS) setup was used to investigate bone ingrowth in a standardized rabbit tibiae implant model, integrated for 7 and 14 weeks.

2. Methods

2.1. Implants and surgical procedure

The implant model consisted of cylindrical Ti6Al4V coin-shaped implants (Ø 5 mm, height 3 mm, Titanium Services SAS, Vourles, France) blasted with titanium dioxide particles to induce an average surface roughness of Sa = 3.46 ± 0.25 µm. Eight implants were inserted into the proximal-medial part of the right tibia of eight New Zealand white rabbits (6 months old, > 3.5 kg) (Figure 1A). To do so, the cortical bone surface was levelled and a cavity was created using a Ø 5.6 mm drill (Dremel Europe, Breda, Netherlands), guided by a central transcortical hole made with a Ø 1.0 mm drill (Figure 1B). Two irrigation holes (Ø 0.9 mm) were drilled through the cortex to allow blood flow towards the interface. Each implant was isolated from existing mature bone by a polytetrafluoroethylene (PTFE) cap (Isoflon, Diemoz, France), to limit bone tissue growth on its sides. This cap was designed to create a 200 µm-thick bone chamber, empty at implantation, between existing cortical bone and the implant surface, where new bone formation could occur. After insertion in the cavity, the implant was stabilized using two orthodontic elastic strings placed in a crossed pattern, and fastened using four Ø 1.6 mm screws (Easy Implant, Chavanod, France) (Figure 1A). Animal handling was approved by the ethical committee of ENVA (École Nationale Vétérinaire d'Alfort) and the requirements of The European Guidelines for Care and Use of Laboratory Animals were followed. Animals were euthanized with an overdose of pentobarbital after 7 weeks (n = 4) and 13 weeks (n = 4) of healing time. Distal tibiae were then carefully dissected with the implants in place. This animal model developed by our group is now well established and has been previously used to investigate various mechanical properties of the bone-implant interface [11,35–37].

2.2.Sample preparation

To access the interface without damaging it, the specimens were fixed in 10 % phosphate-buffered formalin for 1 week, then rinsed with water, dehydrated in ethanol, cleared in xylene and finally embedded in polymethyl methacrylate (PMMA) (VWR International, Fontenay-sous-bois, France) [38,39].

The embedded specimens were then cut transversally in the middle of the implant (Figure 1B) with a diamond wire saw (model 4240, WELL Diamond Wire Saws LA, Mannheim, Germany) to generate 200 µm thick slices. The thickness was further reduced to around 100 µm by manual polishing with abrasive paper SiC foils down to grit 1200 (Accustop and LabPol-5, Struers® ApS, Ballerup, Denmark).

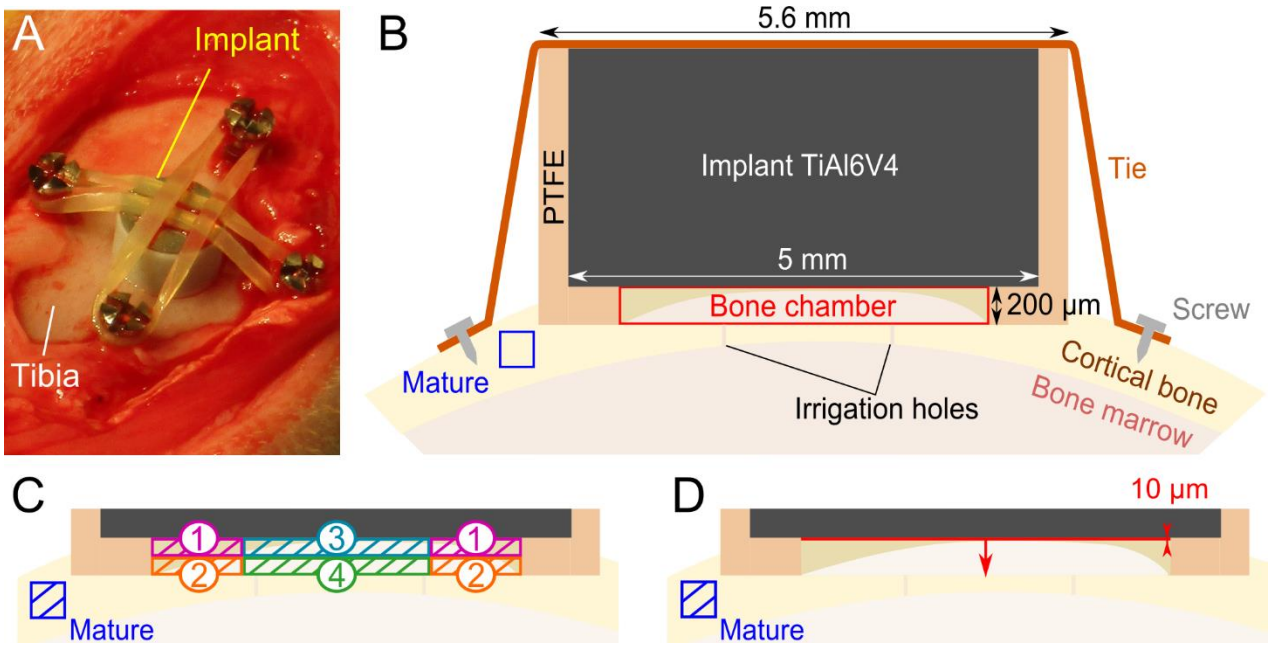

Figure 1 - A: Photography of an implant inserted in the proximal-medial rabbit tibia. B: Schematic description of a transversal cross-section of the coin-shaped implant model and the two scanned regions, i.e. the mature region of interest (ROI) (blue box in the cortex) and the newly formed bone in the bone chamber ROI (red box). C: Bone chamber divided into 4 rectangular ~2000 x 100 µm² ROIs, where ROI 1 corresponded to the lateral chamber close to the implant surface (corners), ROI 2: lateral chamber away from the surface, ROI 3: central chamber close to the implant surface, and ROI 4: central chamber away from the surface. D: the bone chamber was divided into 20 ROIs representing 10 µm-thick horizontal bands parallel to the implant surface (red line).

2.3.Scanning small-angle X-ray scattering (SAXS)

Measurements were carried out using the scanning SAXS [40] micro-focused setup [41] at the cSAXS beamline, Swiss Light Source, Paul Scherrer Institut (PSI), Villigen, Switzerland. A microscope calibrated with the beam was used to define, per specimen, a large region of interest (ROI) over the entire bone chamber (around 4000 x 250 µm²) and a smaller ROI in the cortex representing mature bone tissue (approximately 500 x 500 µm²) (Figure 1B). Two specimens were also scanned over a larger ROI to derive an overview of the crystal properties.

A monochromatic beam of 12.4 keV (λ = 0.999 Å) was focused to about 3.5 µm (vert.) × 4.7 µm (hor.) using Fresnel zone plate of 717 µm diameter and 250 nm outermost zone width [41] and central stop of 160 µm. At every point of the raster scan, a SAXS pattern was recorded using PILATUS 2M detector [42] with 1475 x 1679 pixels² (172 x 172 µm²) in the q-range of 0.02 - 1.45 nm^{-1} placed 7.099 m from the sample. A flight tube under vacuum was placed between the sample and detector to reduce absorption and parasitic scattering from air. To block the direct beam and avoid saturation of the detector at very low scattering angles we used two beam stops, a Ø 3 mm round beam stop and a 3 x 5 mm² rectangular beam stop. Scanning was performed with the step size (pixel size) of 5 µm and an exposure time of 100 ms per scan point. Calibration of detector distance was carried out using AgBH standards.

2.4.Data analysis

The 2D scattering patterns acquired at each scan point were analysed using in-house Matlab® codes (R2018b, MathWorks Inc., MA, USA), as earlier described [23] based on the methods presented by Bünger et al. [43]. Briefly, the scattering patterns were radially integrated over the whole q-range and azimuthally from 0 to 360° in order to obtain the I(q) and the I(θ) scattering curves, respectively [40]. From the I(q) curves, the average mineral crystal thickness (T) was obtained by using weighted iterative curve fitting in the 0.32 - 1.40 nm^{-1} q-range, as previously described [43] ; the quality of the fit was examined by means of the residuals. By fitting a Gaussian curve to the two symmetrical peaks from the I(θ) curves, the average predominant mineral plate orientation (direction of the crystallographic *c*-axis) was determined [44]. Repeated over all scanned points, maps of mineral crystal thickness, plate orientation and degree of orientation were generated for each specimen. A threshold based on integrated SAXS intensity values was applied to remove the background and analyse bone tissue only.

From the maps, the values of the mineral crystal thickness and plate orientation were averaged over different ROIs, for each specimen. Mature control bone was analysed by averaging values from the cortex area. The newly formed tissue inside the bone chamber was analysed as a whole (Figure 1B) and further divided into multiple ROIs following two configurations. First, the chamber was divided into 4 rectangular ROIs of approximately 2000 x 100 μm^2 (Figure 1C) representing the corners region (lateral and close to the implant surface, ROI1), lateral and away from the surface (ROI2), central and close to the surface (ROI3), and central and away from the surface (ROI4). Second, the bone chamber was divided into 20 ROIs corresponding to 10 µm thick horizontal bands parallel to the implant surface (Figure 1D).

Moreover, for all bone chamber ROIs described above, bone content was estimated from the Bone Area/Total Area (BA/TA) ratio, i.e., the number of pixels corresponding to bone over the total number of pixels in the ROI.

2.5.Micro-tomographic imaging

To complement the detailed 2D SAXS investigation of the bone structure within the chamber at the microscale, we conducted 3D micro-tomographic imaging on two specimens (7 weeks and 13 weeks of healing), prepared following the same *in vivo* procedure (see section 2.1). Specimens were imaged intact (non-embedded and unsliced) at the X02DA TOMCAT beamline (SLS, PSI, Switzerland) using a monochromatic beam energy 30 keV, 5.5 μm^3 voxel size, 3000 projections over 180° and 12 ms exposure time. Due to artefacts induced by the metal implants, the scans were manually segmented to quantify bone ingrowth inside the chamber using Seg3D (SCI Institute's NIH/NIGMS CIBC Center). Scans were qualitatively examined and bone volume fraction (Bone Volume (BV) / Total Volume (TV)) was quantified in 3D in similar 4 ROIs as presented above (see Figure 1C) (BoneJ plugin [45], ImageJ [46]).

2.6.Statistical analysis

Mean mineral crystal thickness, plate orientation and BA/TA were determined for each ROI and specimen for a given healing time point. Using non-parametric Mann-Whitney U tests, the temporal evolution was evaluated for each ROI between 7 weeks and 13 weeks of healing time, and the spatial evolution was investigated by comparing ROIs among each other, for a given time point. All tests were performed between two groups or two ROIs at the time, and used a significance level of $p = 0.05$ (R2018b, MathWorks Inc., MA, USA).

3. Results

3.1.Overview within the chambers

Both after 7 weeks and 13 weeks of healing time, the mineral crystal thickness in the bone chamber (1.8 ± 0.45 nm and 2.4 ± 0.57 nm respectively) were significantly lower ($p = 0.014$ and $p = 0.028$) compared to that of mature cortical bone tissue (2.5 ± 0.21 nm and 2.8 ± 0.35 nm respectively) (Figure 2B). Thus, the mineral crystal thickness increased by around 30% within the bone chamber over the 6 weeks of osseointegration ($p = 0.014$) (Figure 2A and Suppl1). However, it remained similar within the mature regions ($p > 0.05$) (Figure 2B). The mineral crystal thickness values were more heterogeneous (larger standard deviation) in the bone chamber compared to the mature regions after 13 weeks ($p = 0.014$) (Figure 2C).

The bone chambers were partially filled with newly formed bone tissue throughout osseointegration, as shown by a significant increase in BA/TA between 7 weeks (14 ± 6 %) and 13 weeks (36 ± 15 %) (Figure 2A, D, Suppl1).

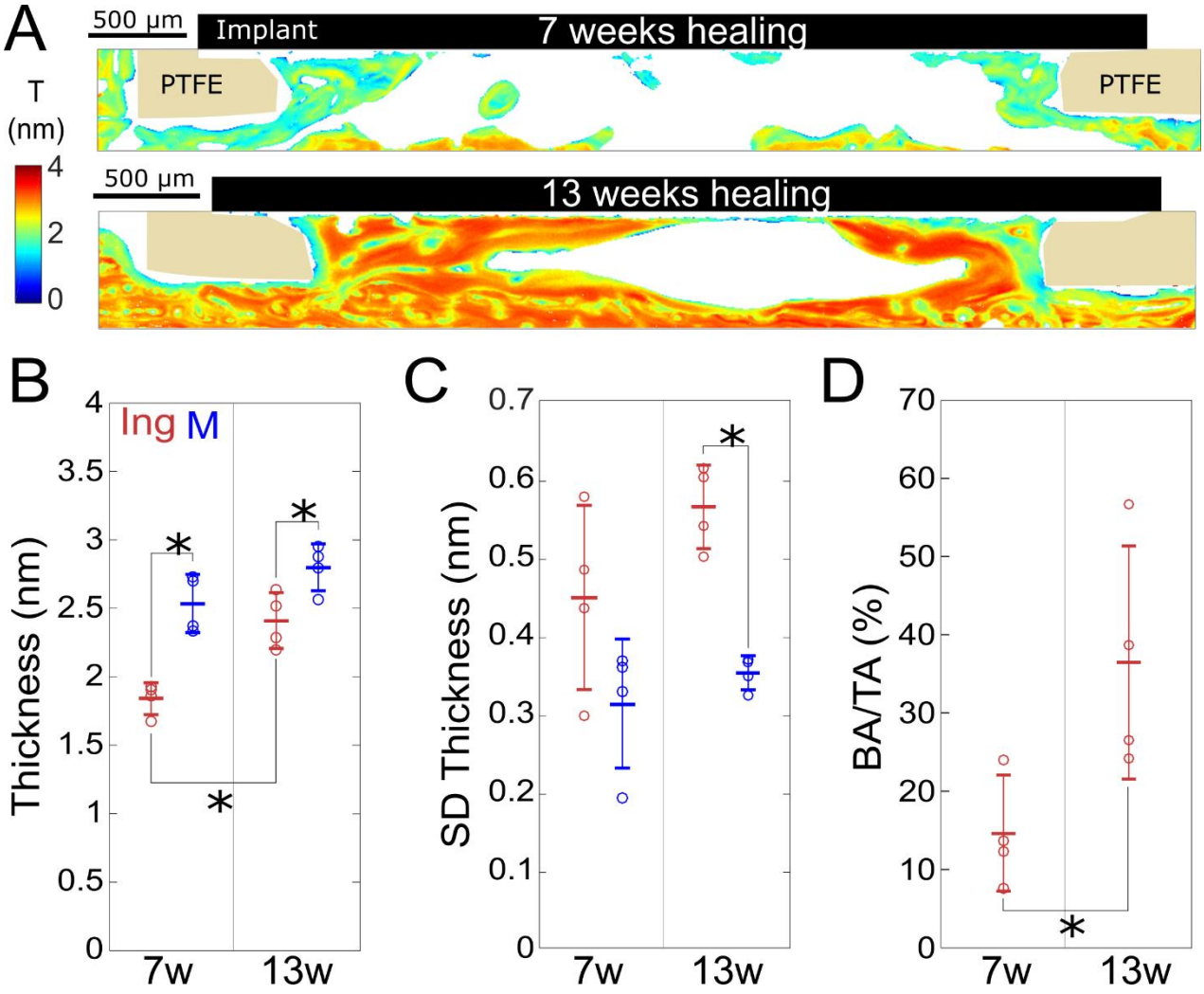

Figure 2 – A: Overview of mineral crystal thickness (T) maps for typical 7 weeks (top, Specimen S1) and 13 weeks specimens (bottom, Specimen S5). See Suppl1 for all maps. Average thickness (B), standard deviation (SD) of thickness values (C) and BA/TA (D) in the bone chamber (Ing for ingrowth, red) and mature (M, blue) regions. Data is presented as mean ± SD, with all specimen values (dots). Only significant differences (, $p < 0.05$) are identified.*

3.2.Spatial variation within the bone chamber

After 7 weeks of osseointegration, crystals close to the PTFE and away from the implant surface (ROI2) were significantly thicker than the other ROIs. Moreover, crystals in the central region, close to the implant surface (ROI3) were significantly thinner (except compared to ROI4, which contained only limited data, p = 0.07) (Figure 3A). Crystals in all ROIs were found to be significantly thinner than those of the corresponding mature regions. After 13 weeks, a global increase in thickness was observed (non-significant for the away-central ROI4, due to limited data points), towards the values of mature regions (only values ROI1 and ROI3, close to the implant, stayed significantly lower, p = 0.014) and differences among regions decreased.

Bone distribution was uneven throughout the chamber, with most of the bone tissue being found in the corners (ROI1, significant after 7 weeks except with ROI2, p = 0.057), and the least, if not any, found further away from the implant in the centre of the chamber (ROI4, close to the cortical bone) (Figure 3B, Suppl1). A global increase in bone ingrowth during healing was noted for all regions though being significant for only ROI3, with more heterogeneity in the bone content among the specimens after 13 weeks (Figure 3B).

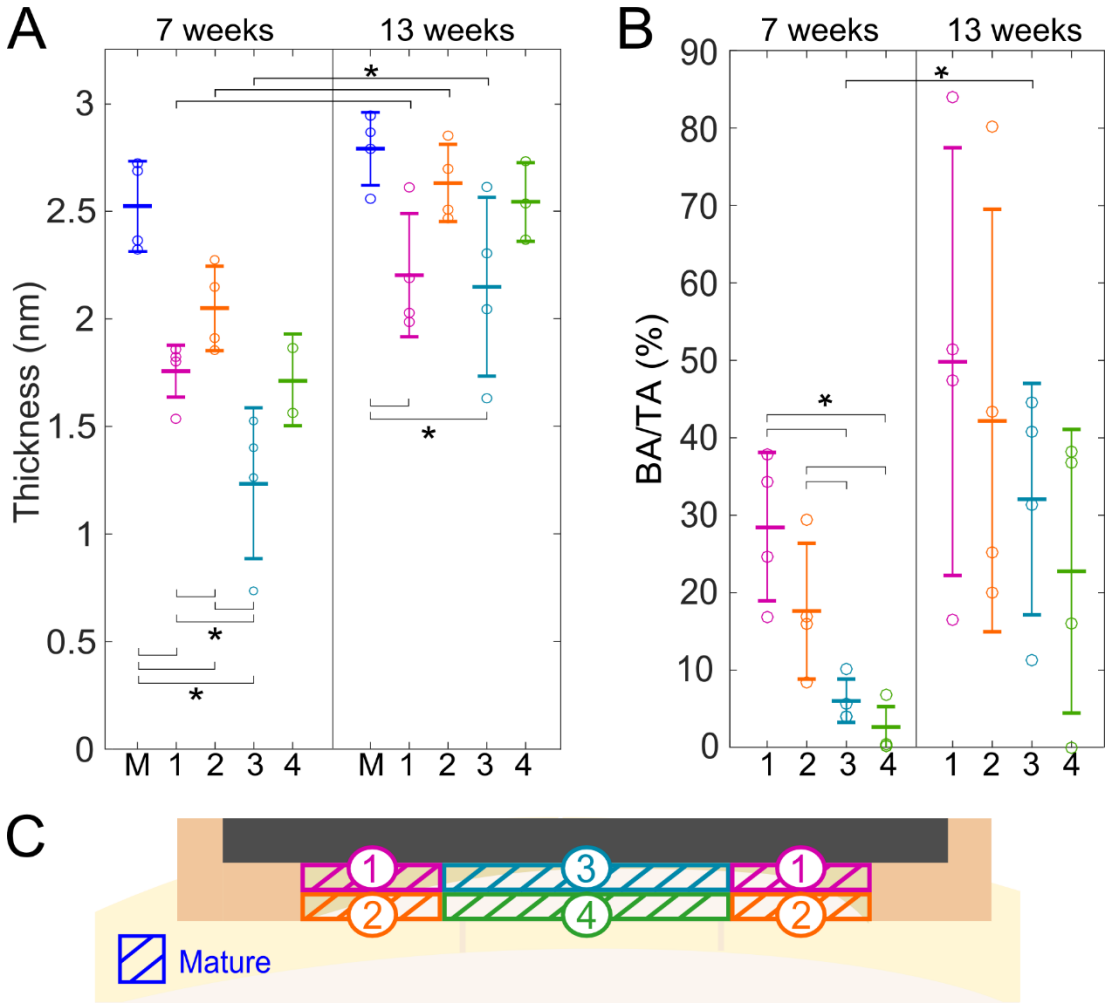

*Figure 3 - Spatial and temporal evolutions of average crystal thickness (A) and bone content (B) in the bone chamber according to analysis within 4 rectangular sub-regions of interest (ROI) (C). M: mature ROI, 1: lateral chamber close to the implant surface ROI (corners), 2: lateral chamber away from the surface ROI, 3: central chamber close to the implant surface ROI, and 4: central chamber away from the surface ROI. Data is presented as mean ± SD, with all specimen values as dots. Only significant differences (p < 0.05) are identified as *.*

3.3.Evolution from the implant surface

Refined analysis within 10 µm-thick bands parallel to the implant surface revealed a progressive increase in mineral crystal thickness when going from the implant surface to the end of the bone chamber (cortical bone interface) (see Figure 1D, Figure 4A). For both time points, a fast thickening of the crystals (rate of ~0.01 nm/µm) was observed in the first 100 µm, and mineral crystal thicknesses were plateauing further away from the implant surface (Figure 4A). After 7 weeks of integration, thicknesses increased from an average of 1.06 ± 0.45 nm at the implant surface to 1.92 ± 0.16 nm at 100 µm away (+ 80 %) ($p = 0.014$). The same tendency was observed at 13 weeks, with globally thicker crystals, and values increasing from 1.55 ± 0.07 nm to 2.48 ± 0.15 nm (+ 60%) ($p = 0.014$) (Figure 4A). Mineral crystal thickness was lower in all ingrowth bands compared to the corresponding mature region, significant at 7 weeks (except the band furthest away from the implant) and with lower differences at 13 weeks (only significant up to 120 µm from the implant).

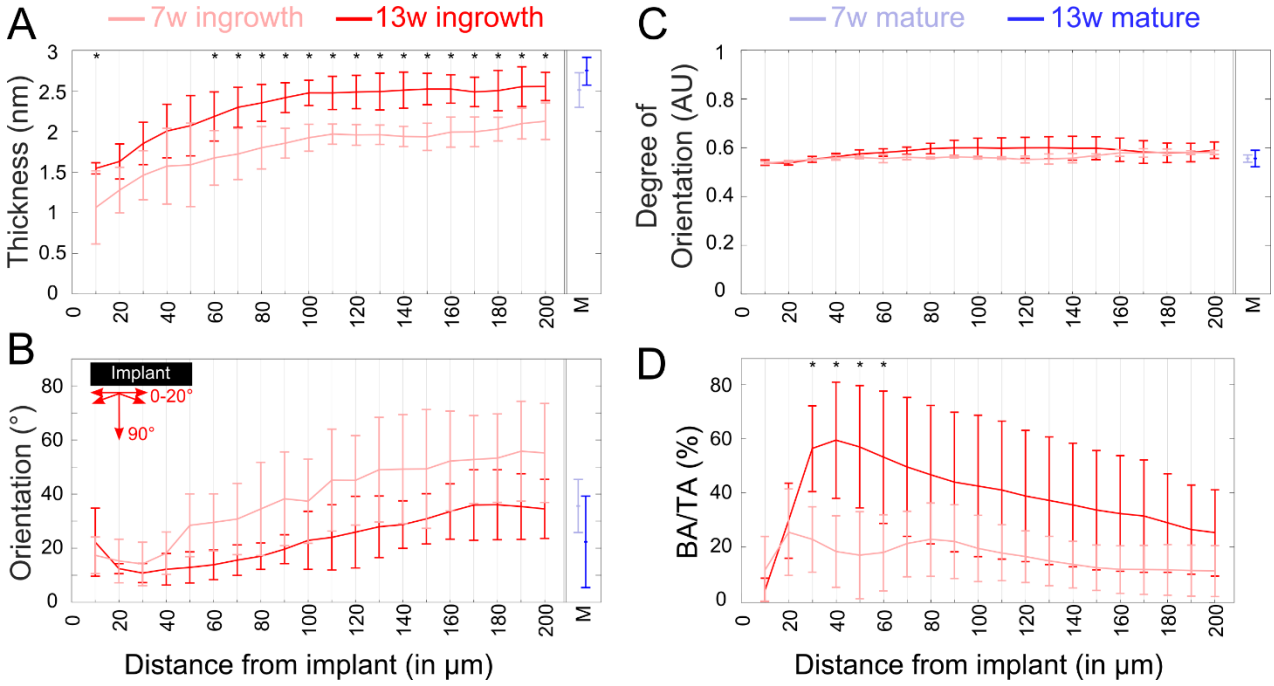

*Figure 4 - Evolution of average crystal thickness (A), plate orientation (B), degree of orientation (C) and bone content (BA/TA, D), within 10 µm thick bands from the implant surface (see Figure 1D), presented as mean and standard deviations. 7w data points are presented in pink, 13w time points in red, and corresponding mature (M) values in light and dark blue, respectively. Significant differences ($p<0.05$) between 7 and 13 weeks are identified as * (for a given ROI).*

Mineral platelets were more oriented close to the implant surface in the first 50 µm ($p < 0.05$ compared to mature at 7 weeks), with an average orientation below 20°, where 0° is parallel to the implant surface (Figure 4B). Further away from the implant, plate orientation gradually became more heterogeneous (higher average values and larger standard deviations). Mineral plate orientations in mature bone also presented relatively large variations; it has to be noted that the specimens were cut radially, and that the degree of orientation was constant and moderate (around 0.6, Figure 4C, a score where 1 is fully aligned [44]).

A global increase in bone content was observed during osseointegration, significant only for ROIs between 30 and 60 µm from the implant surface. After 13 weeks, the first 20µm close to the surface as well as the regions furthest away from the implant contained less bone (10 - 30 %, Figure 4D) ($p < 0.05$, compared to the maximum at 40 µm).

3.4.3D bone distribution

The 3D tomographic reconstructions of the two unsliced samples (Figure 5) and BV/TV quantifications supported the bone distribution trends that were quantified in 2D slices (Figure 3B). For both specimens, most of the bone was present in the corners (equivalent of ROI1 in Figure 1C) with a BV/TV of 60 % and 64 % for 7 weeks' and 13weeks' specimens respectively. Bone was also present close to the PTFE crown and the mature bone (equivalent of ROI2), with a BV/TV of 54 % in both specimens. Less tissue was present in the central region close to the implant (equivalent of ROI3), where BV/TV of 15 % and 18 % were found, and only small amount of bone in the away-central region (equivalent of ROI4).

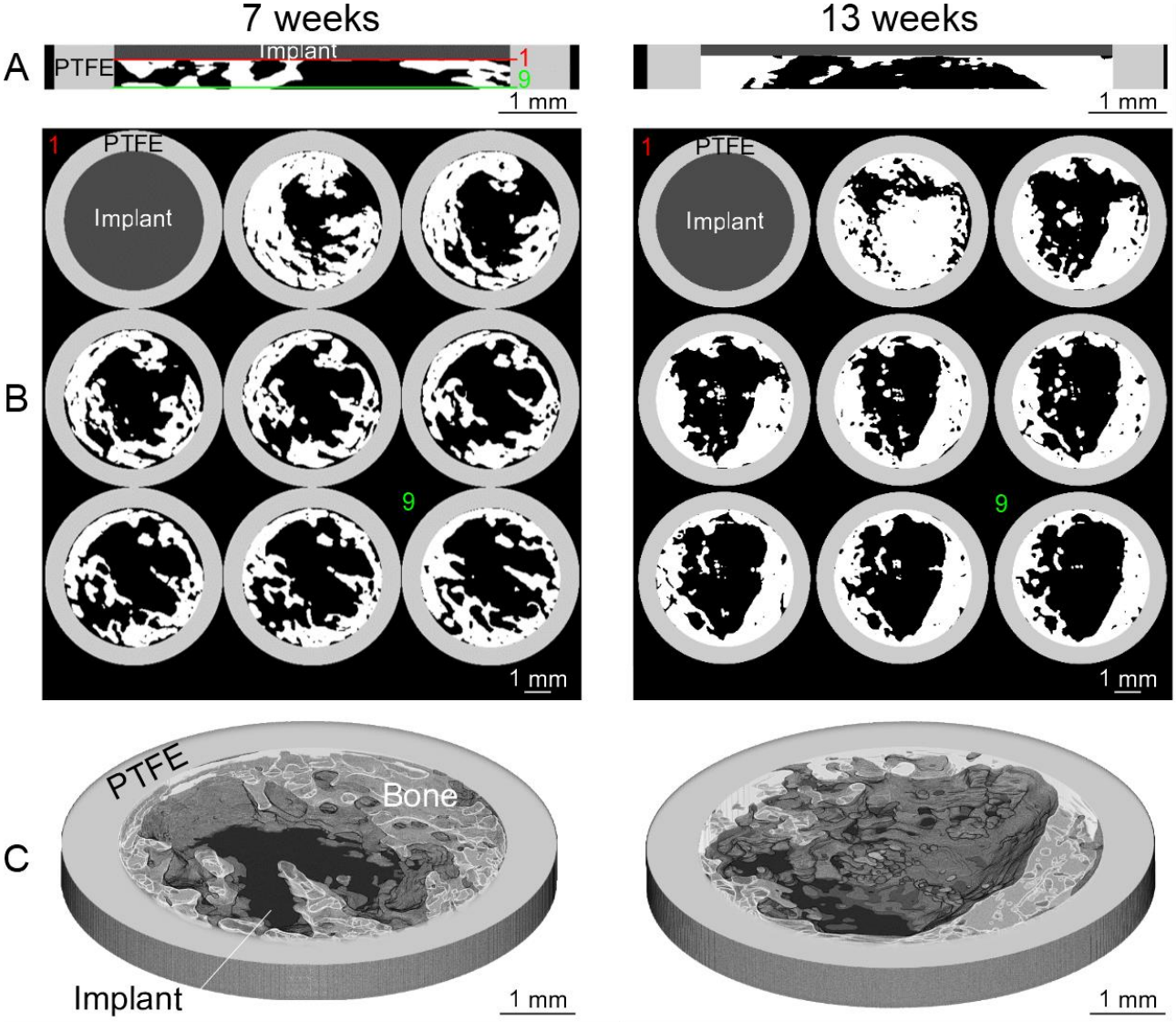

Figure 5 - Bone segmentation (white) inside the PTFE chamber (light grey) of similar samples after 7 weeks (left) and 13 weeks (right) of healing. 2D slices (A) extracted from the middle of the stack, corresponding to the orientation of the analysed SAXS slices (e.g., Figure 1B). Montages (B) representing sequential slices parallel to the implant surface, from within the implant (slice 1, dark grey) to the end of the chamber (slice 9), every ~30 µm. 3D renderings (C) of the bone chambers, to appreciate bone distribution (the implant is in black in the bottom).

4. Discussion

Advancing knowledge about how the bone ultrastructure adapts to an implant is crucial to better comprehend the biomechanical properties of the newly formed bone-implant interface and represents a first step to understand why and how an implant could later loosen and fail. Thorough investigations of both spatial and temporal evolutions of bone ingrowth with respect to how the mineral crystals are formed, oriented and re-shaped in close proximity to a metallic implant is missing in the available literature. This study represents one of the first to investigate the evolution of newly formed bone ultrastructure around a titanium surface using a micro-focused SAXS setup and a bone chamber model. Spatial analyses revealed thicker mineral crystals close to the chamber walls and away from the interface. Thin crystals were observed in the close vicinity of the implant, quickly increasing in thicknesses during the first 100 μm moving away from the surface. Moreover, with increasing healing time, an overall thickening of the mineral crystals was observed, together with increased bone tissue formation.

The average mineral crystal thickness values obtained in this study (ranging from 1.8 to 2.8 nm) are consistent with the ones found in the literature. Mineral crystal thickness increased with age in a similar animal model [30], from 1.6 nm in new-born to 2.5 nm in 6-month-old rabbit cortical bone. The average mature bone crystal thickness of 2.5 - 2.8 nm measured here (Figure 2) is consistent with literature data, where thickness from 2.5 nm [30] to 3.6 nm [47] have been reported for rabbit mature bone of similar age. Moreover, newly formed bone values within the chamber (e.g. 1.8 nm at 7 weeks) are similar to young rabbit bone (e.g. 1.8 nm for 4-week-old rabbits) [30]. The method used in this study to estimate the crystal thickness has earlier been widely used [23,30,44,48].

Young and immature tissue in the bone chamber

Within the bone chamber, crystals were on average thinner than the ones in the mature bone cortex, suggesting that the bone tissue was still young and immature. This is consistent with literature, where thinner crystals were measured in close proximity to metallic pins [16,49] and scaffolds [31], as well as in fracture healing studies where newly formed bone presented thinner crystals compared to mature regions [24,44]. Studies focusing on resorbable materials have depicted either thinner or thicker mineral crystals in newly formed bone, a discrepancy that could be attributed to potential chemical effects on the bone during degradation [27,32–34]. Moreover, we observed an increase in mineral crystal thickness in the bone chamber with increasing healing time (from 1.8 ± 0.45 nm to 2.4 ± 0.57 nm) consistent with a maturation of the bone tissue. This result is in agreement with the literature on bulk bone, where an increase in thickness and length of crystals with age has been reported [30,50] as well as during bone healing [24,44]. However, a recent study that investigated bone formation around Titanium and resorbable screws in rats did not report any differences in platelet thickness with healing nor compared to mature bone [51]. This discrepancy could be explained by their limited sample size, different sample preparation strategies (difficulties in slicing a metal implant), as well as different data analysis approaches. Indeed, mineral crystal thickness can be extracted using different methods, such as the stack of card model assuming preferential direction and equal degree of mineralization [52], which may be limited when investigating newly formed bone tissue, of heterogeneous structure. The curve-fitting approach used in this manuscript is independent of any assumption on mineral volume fraction or preferred direction for the mineral crystals.

The mineral crystal thickness was more heterogeneous in the newly formed bone compared to the mature regions after 13 weeks (Figure 2C). This can be explained by the dynamic process of both remodelling, i.e. existing bone matures (increase in crystal thickness), and ongoing new bone formation (thinner crystals). This result is supported by visual observation of the crystal thickness maps (Figure 2A, bottom) where thicker crystals are observed in the centre of the bone structure and thinner crystals at the edges.

Understanding the evolution of mineral crystal thicknesses at the interface can help comprehend the tissue mechanical properties. Nanoindentation campaigns measured lower elastics properties in newly formed bone around titanium implants compared to mature bone [35,53,54]. A relationship between mineral crystals thickness and elastic properties of bone tissue has been suggested for rabbit cortical bone [30], but only limited data has been gathered in the proximity of a metallic implant. A former nanoindentation campaign conducted by our team on similar specimens confirms this relationship, as lower indentation moduli were measured in the bone chambers, along with an increase during healing [35].

Implant affects the bone nanostructure up to 100 µm

The evolution in 10 µm thick bands from the implant surface outwards revealed thinner minerals close to the implant surface, and a sharp linear increase in thickness in the first 100 µm (Figure 4). This focus on the mineral crystal thickness distribution at the bone-implant interface (50 - 100 µm from the implant surface) was possible thanks to the micro-focused SAXS setup – beamsize of 3.5 µm (vert.) × 4.7 µm (hor.) - as compared to earlier studies in the literature – beamsizes of 50 to 250 µm [16,31,49]. To our knowledge, only Bünger et al. [31] have previously investigated the spatial evolution of mineral crystals thickness around titanium and tantalum scaffolds (50 µm beam size), with findings consistent with our observations. In addition to thinner crystals, we also observed crystals being more aligned along the implant surface within the first 50 µm (Figure 4), consistent with previous SAXS studies where crystals have been observed to align circumferentially to Titanium rods [16,49] and along the surface of Titanium scaffolds [31]. Collagen fibers, following the same orientation as mineral plates, have also been observed to align in the first micrometres along the surface of extracted dental implants, using electron microscopy [55]. Both these findings, i.e. thinner and aligned plates, suggest that the implant surface influences the structure and orientation of the bone ultrastructure within approximately 100 µm of a metallic implant. Together with less bone tissue observed in the close vicinity of the implant, this could consequently affect the binding to the interface. This could rise from the gap in mechanical properties between Titanium (Young modulus roughly 100-120 GPa [56]) and newly formed bone tissue (around 2 to 12 GPa based on nanoindentation [35,57]) which leads to a localized heterogeneous mechanical environment [58,59] and may affect mechanostransduction, and thereby also osseointegration [3]. These results are also supported by nanoindentation measurements [60], with lower indentation moduli measured close to dental implants, at an increasing linear rate of 0.014 GPa/µm until approximately 150 µm, before mechanical properties were observed to plateau.

A combination of distant and contact osteogenesis

A subdivision into four regions of interest (ROI) within the bone chamber (Figure 3) enabled us to understand the growth kinetics of bone healing in this model (see Figure 6). More bone was observed close to the PTFE crown, both in the 2D slices (Figure 3B) as well as in the 3D rendering from X-ray microtomography of similar samples (Figure 5). This could be explained by a combination

of contact and distance osteogeneses, in accordance with previous findings in bone chamber models [10]. First, the slightly higher bone content in the corners (ROI1 in Figure 3B) could be consistent with contact osteogenesis, i.e. bone formation in contact with the implant, potentially facilitated by the design of the model, where the surfaces could promote bone cells migration [61,62], and the blood containing osteogenic cells could accumulate in the corners [63]. Second, the thicker crystals observed in regions close to existing mature bone (ROI2 in Figure 3A) would suggest older bone, and would be consistent with distance osteogenesis, where bone forms by apposition onto existing mature bone. The healing process would thus proceed with tissue remodelling in the corners together with apposition of new bone from the mature cortex inwards, along with bone starting to colonize the central implant surface (Figure 6). At last, a bridging with the mature cortex in the centre of the chamber would occur, where only limited bone was seen (Figure 3, Figure 5). The observed differences in crystal thicknesses and the suggested kinetics of ingrowth are consistent with recent mechanical data gathered with nanoindentation and micro-Brillouin scattering techniques on sequential slices to the ones analysed here, where higher elastic properties were measured at the chambers' edges (unpublished data). Earlier healing time points will be investigated in the future to validate such hypothesis.

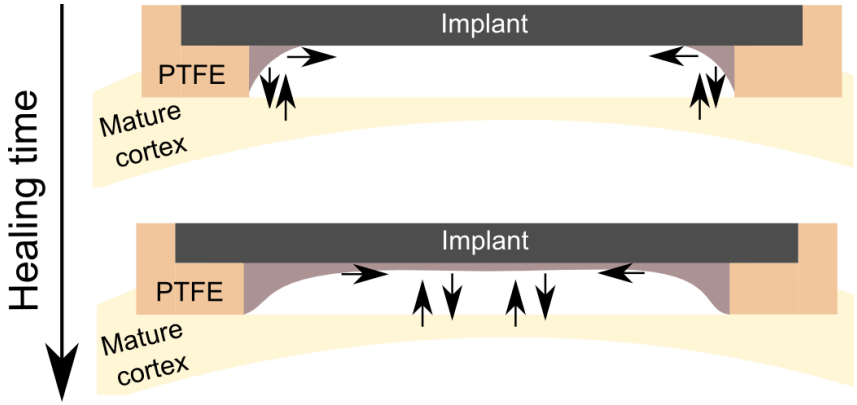

Figure 6 – Schematic description of bone ingrowth kinetics in the chamber, the arrows illustrate the main directions of bone growth.

The limitations of this study include a low number of specimens (n = 4 per group). However, this still represents the largest and most refined SAXS study investigating spatial evolution of bone mineral crystal thickness at the bone-implant interface. Only crystals diffracting in the beam direction contributed to the average thickness and orientation measured here, which limits the analysis to the currently analysed radial direction; this will be extended through other cutting directions in the future, particularly along the longitudinal direction, where bone presents a higher degree of orientation [30]. We did not correct for sample transmission or thickness as both parameters were similar among specimens. Moreover, as neither of the reported parameters is directly dependent on absolute intensity, this did not affect the comparisons performed in this study. To focus on the bone-metal interface, the bone chamber was designed with a PTFE crown, considered inert to bone [64] and with lower mechanical properties thus preventing any stress-shielding. Still, this crown could have influenced the results and further studies will explore such effect and investigate the use of other inert materials. The slight increase in control mature values –non-significant) could rise from the surgery or ongoing growth of the animals, and will be corrected in further studies also assessing the contralateral non-operated limbs. Sample preparation was challenging as thin slices of bone together with a metallic implant are difficult to prepare, and thicker slices are not compatible with diffraction measurements. Therefore, 100 µm-thickness were selected as a trade-off, being sufficiently thin, while ensuring that all interfaces

remained intact without debonding. Finally, this study focused on early implant stability and the evolution of the bone-implant interface within the first weeks after surgery. Further studies involving different models would be needed to explore how the biomechanical properties of the interface evolve along bone remodelling and adapt to e.g., changes in loading patterns [3,65].

5. Conclusions

This represents the first micro-focused SAXS study that investigated both spatial and temporal evolutions of mineral crystal thickness and plate orientation at the bone-implant interface. With a standardized bone chamber model, we could isolate newly formed bone presenting thinner mineral crystals compared to mature tissue, and observed the thickening of the crystals during healing as bone matures and is being remodelled. The micro-resolution setup enabled a refined analysis close to the implant surface, where an approximate 100 µm-thick bone tissue layer presented thinner crystals oriented along the implant surface, rapidly thickening and displaying less alignment moving further inside the bone chamber. This immature bone layer suggests an ongoing osseointegration, with potentially still weak mechanical properties. Crystal thickness appears to be a sensitive parameter to follow and attest of good osseointegration. Further detailed studies are required to deepen the investigation of bone ultrastructure close to implants, especially concerning the adaptation of the interface to mechanical loading.

6. Acknowledgments

This project has received funding from the European Union's Horizon 2020 research and innovation programme under the Marie Sklodowska-Curie grant agreement No 797764. This project has received funding from the European Research Council (ERC) under the European Union's Horizon 2020 research and innovation program (grant agreement No 682001, project ERC Consolidator Grant 2015 BoneImplant). We acknowledge the Paul Scherrer Institut, Villigen, Switzerland for provision of synchrotron radiation beamtime at the cSAXS beamline X12SA as well as at the TOMCAT beamline X02DA of the SLS, and we thank Vladimir Novak for the provided help for tomographic imaging, conducted during another beamtime. M.V. acknowledges funding by European Union's Horizon 2020 research and innovation program under the Marie Skłodowska-Curie grant agreement No 701647, as well as SNSF grant No 200021L_169753.

7. References

[1] B.R. Chrcanovic, J. Kisch, T. Albrektsson, A. Wennerberg, Factors Influencing Early Dental Implant Failures, J. Dent. Res. 95 (2016) 995–1002. https://doi.org/10.1177/0022034516646098.

[2] K. Grisar, D. Sinha, J. Schoenaers, T. Dormaar, C. Politis, Retrospective Analysis of Dental Implants Placed Between 2012 and 2014: Indications, Risk Factors, and Early Survival, Int. J. Oral Maxillofac. Implants. 32 (2017) 649–654. https://doi.org/10.11607/jomi.5332.

[3] L. Amengual-Peñafiel, M. Brañes-Aroca, F. Marchesani-Carrasco, M.C. Jara-Sepúlveda, L. Parada-Pozas, R. Cartes-Velásquez, Coupling between Osseointegration and Mechanotransduction to Maintain Foreign Body Equilibrium in the Long-Term: A Comprehensive Overview, J. Clin. Med. 8 (2019). https://doi.org/10.3390/jcm8020139.

[4] T. Albrektsson, B. Chrcanovic, P.-O. Östman, L. Sennerby, Initial and long-term crestal bone responses to modern dental implants, Periodontol. 2000. 73 (2017) 41–50. https://doi.org/10.1111/prd.12176.

[5] G. Haïat, H.-L. Wang, J. Brunski, Effects of Biomechanical Properties of the Bone–Implant Interface on Dental Implant Stability: From In Silico Approaches to the Patient's Mouth, Annu. Rev. Biomed. Eng. 16 (2014) 187–213. https://doi.org/10.1146/annurev-bioeng-071813-104854.

[6] A.J. Wirth, J. Goldhahn, C. Flaig, P. Arbenz, R. Müller, G.H. van Lenthe, Implant stability is affected by local bone microstructural quality, Bone. 49 (2011) 473–478. https://doi.org/10.1016/j.bone.2011.05.001.
[7] A. Palmquist, A multiscale analytical approach to evaluate osseointegration, J. Mater. Sci. Mater. Med. 29 (2018). https://doi.org/10.1007/s10856-018-6068-y.
[8] X. Gao, M. Fraulob, G. Haïat, Biomechanical behaviours of the bone–implant interface: a review, J. R. Soc. Interface. 16 (2019) 20190259. https://doi.org/10.1098/rsif.2019.0259.
[9] H.J. Rønold, J.E. Ellingsen, The use of a coin shaped implant for direct in situ measurement of attachment strength for osseointegrating biomaterial surfaces, Biomaterials. 23 (2002) 2201–2209. https://doi.org/10.1016/s0142-9612(01)00353-2.
[10] T. Berglundh, I. Abrahamsson, N.P. Lang, J. Lindhe, De novo alveolar bone formation adjacent to endosseous implants, Clin. Oral Implants Res. 14 (2003) 251–262. https://doi.org/10.1034/j.1600-0501.2003.00972.x.
[11] V. Mathieu, R. Vayron, E. Barthel, D. Dalmas, E. Soffer, F. Anagnostou, G. Haiat, Mode III cleavage of a coin-shaped titanium implant in bone: effect of friction and crack propagation, J. Mech. Behav. Biomed. Mater. 8 (2012) 194–203. https://doi.org/10.1016/j.jmbbm.2011.12.012.
[12] T.M. Shea, J. Laun, S.A. Gonzalez-Blohm, J.J. Doulgeris, W.E. Lee, K. Aghayev, F.D. Vrionis, Designs and techniques that improve the pullout strength of pedicle screws in osteoporotic vertebrae: current status, BioMed Res. Int. 2014 (2014) 748393. https://doi.org/10.1155/2014/748393.
[13] S. Le Cann, Tudisco, M. Turunen, A. Patera, R. Mokso, M. Tägil, O. Belfrage, S.A. Hall, H. Isaksson, Investigating the Mechanical Characteristics of Bone-Metal Implant Interface Using in situ Synchrotron Tomographic Imaging, Front. Bioeng. Biotechnol. 6 (2019). https://doi.org/10.3389/fbioe.2018.00208.
[14] K. Grandfield, Bone, implants, and their interfaces, Phys. Today. 68 (2015) 40–45. https://doi.org/10.1063/PT.3.2748.
[15] F.A. Shah, X. Wang, P. Thomsen, K. Grandfield, A. Palmquist, High-Resolution Visualization of the Osteocyte Lacuno-Canalicular Network Juxtaposed to the Surface of Nanotextured Titanium Implants in Human, ACS Biomater. Sci. Eng. 1 (2015) 305–313. https://doi.org/10.1021/ab500127y.
[16] R.M. Hoerth, M.R. Katunar, A. Gomez Sanchez, J.C. Orellano, S.M. Ceré, W. Wagermaier, J. Ballarre, A comparative study of zirconium and titanium implants in rat: osseointegration and bone material quality, J. Mater. Sci. Mater. Med. 25 (2014) 411–422. https://doi.org/10.1007/s10856-013-5074-3.
[17] L.A. Giannuzzi, D. Phifer, N.J. Giannuzzi, M.J. Capuano, Two-Dimensional and 3-Dimensional Analysis of Bone/Dental Implant Interfaces With the Use of Focused Ion Beam and Electron Microscopy, J. Oral Maxillofac. Surg. 65 (2007) 737–747. https://doi.org/10.1016/j.joms.2006.10.025.
[18] N. Reznikov, R. Shahar, S. Weiner, Bone hierarchical structure in three dimensions, Acta Biomater. 10 (2014) 3815–3826. https://doi.org/10.1016/j.actbio.2014.05.024.
[19] P. Fratzl, H.S. Gupta, E.P. Paschalis, P. Roschger, Structure and mechanical quality of the collagen–mineral nano-composite in bone, J. Mater. Chem. 14 (2004) 2115–2123. https://doi.org/10.1039/B402005G.
[20] N. Reznikov, M. Bilton, L. Lari, M.M. Stevens, R. Kröger, Fractal-like hierarchical organization of bone begins at the nanoscale, Science. 360 (2018). https://doi.org/10.1126/science.aao2189.
[21] F.A. Shah, P. Thomsen, A. Palmquist, Osseointegration and current interpretations of the bone-implant interface, Acta Biomater. 84 (2019) 1–15. https://doi.org/10.1016/j.actbio.2018.11.018.
[22] W. Wagermaier, A. Gourrier, B. Aichmayer, Understanding hierarchy and functions of bone using scanning x-ray scattering methods, in: R.W. Peter Fratzl John W.C. Dunlop (Ed.), Underst. Hierarchy Funct. Bone Using Scanning X-Ray Scatt. Methods, RSC publishing, 2013. https://doi.org/10.1039/9781849737555-00046.
[23] M.J. Turunen, J.D. Kaspersen, U. Olsson, M. Guizar-Sicairos, M. Bech, F. Schaff, M. Tägil, J.S. Jurvelin, H. Isaksson, Bone mineral crystal size and organization vary across mature rat bone cortex, J. Struct. Biol. 195 (2016) 337–344. https://doi.org/10.1016/j.jsb.2016.07.005.
[24] N. Mathavan, M.J. Turunen, M. Guizar-Sicairos, M. Bech, F. Schaff, M. Tägil, H. Isaksson, The compositional and nano-structural basis of fracture healing in healthy and osteoporotic bone, Sci. Rep. 8 (2018) 1591. https://doi.org/10.1038/s41598-018-19296-z.

[25] Y. Liu, I. Manjubala, H. Schell, D.R. Epari, P. Roschger, G.N. Duda, P. Fratzl, Size and habit of mineral particles in bone and mineralized callus during bone healing in sheep, J. Bone Miner. Res. Off. J. Am. Soc. Bone Miner. Res. 25 (2010) 2029–2038. https://doi.org/10.1002/jbmr.84.

[26] R.M. Hoerth, B.M. Seidt, M. Shah, C. Schwarz, B.M. Willie, G.N. Duda, P. Fratzl, W. Wagermaier, Mechanical and structural properties of bone in non-critical and critical healing in rat, Acta Biomater. 10 (2014) 4009–4019. https://doi.org/10.1016/j.actbio.2014.06.003.

[27] M.A. Woodruff, C. Lange, J. Reichert, A. Berner, F. Chen, P. Fratzl, J.-T. Schantz, D.W. Hutmacher, Bone tissue engineering: from bench to bedside, Mater. Today. 15 (2012) 430–435. https://doi.org/10.1016/S1369-7021(12)70194-3.

[28] M. Georgiadis, R. Müller, P. Schneider, Techniques to assess bone ultrastructure organization: orientation and arrangement of mineralized collagen fibrils, J. R. Soc. Interface. 13 (2016) 20160088. https://doi.org/10.1098/rsif.2016.0088.

[29] H. Isaksson, M. Malkiewicz, R. Nowak, H.J. Helminen, J.S. Jurvelin, Rabbit cortical bone tissue increases its elastic stiffness but becomes less viscoelastic with age, Bone. 47 (2010) 1030–1038. https://doi.org/10.1016/j.bone.2010.08.015.

[30] E. Törnquist, H. Isaksson, M.J. Turunen, Mineralization of cortical bone during maturation and growth in rabbits, J. Bone Miner. Metab. (2019). https://doi.org/10.1007/s00774-019-01068-y.

[31] M.H. Bünger, M. Foss, K. Erlacher, H. Li, X. Zou, B.L. Langdahl, C. Bünger, H. Birkedal, F. Besenbacher, J.S. Pedersen, Bone nanostructure near titanium and porous tantalum implants studied by scanning small angle x-ray scattering, Eur. Cell. Mater. 12 (2006) 81–91.

[32] T.A. Grünewald, A. Ogier, J. Akbarzadeh, M. Meischel, H. Peterlik, S. Stanzl-Tschegg, J.F. Löffler, A.M. Weinberg, H.C. Lichtenegger, Reaction of bone nanostructure to a biodegrading Magnesium WZ21 implant - A scanning small-angle X-ray scattering time study, Acta Biomater. 31 (2016) 448–457. https://doi.org/10.1016/j.actbio.2015.11.049.

[33] A. Cipitria, W. Wagermaier, P. Zaslansky, H. Schell, J.C. Reichert, P. Fratzl, D.W. Hutmacher, G.N. Duda, BMP delivery complements the guiding effect of scaffold architecture without altering bone microstructure in critical-sized long bone defects: A multiscale analysis, Acta Biomater. 23 (2015) 282–294. https://doi.org/10.1016/j.actbio.2015.05.015.

[34] A. Cipitria, C. Lange, H. Schell, W. Wagermaier, J. Reichert, D. Hutmacher, P. Fratzl, G. Duda, Porous scaffold architecture guides tissue formation, J. Bone Miner. Res. 27 (2012) 1275–1288. https://doi.org/10.1002/jbmr.1589.

[35] R. Vayron, E. Barthel, V. Mathieu, E. Soffer, F. Anagnostou, G. Haiat, Nanoindentation measurements of biomechanical properties in mature and newly formed bone tissue surrounding an implant, J. Biomech. Eng. 134 (2012) 021007. https://doi.org/10.1115/1.4005981.

[36] R. Vayron, M. Matsukawa, R. Tsubota, V. Mathieu, E. Barthel, G. Haiat, Evolution of bone biomechanical properties at the micrometer scale around titanium implant as a function of healing time, Phys. Med. Biol. 59 (2014) 1389–1406. https://doi.org/10.1088/0031-9155/59/6/1389.

[37] V. Mathieu, K. Fukui, M. Matsukawa, M. Kawabe, R. Vayron, E. Soffer, F. Anagnostou, G. Haiat, Micro-Brillouin scattering measurements in mature and newly formed bone tissue surrounding an implant, J. Biomech. Eng. 133 (2011) 021006. https://doi.org/10.1115/1.4003131.

[38] N. Chevallier, F. Anagnostou, S. Zilber, G. Bodivit, S. Maurin, A. Barrault, P. Bierling, P. Hernigou, P. Layrolle, H. Rouard, Osteoblastic differentiation of human mesenchymal stem cells with platelet lysate, Biomaterials. 31 (2010) 270–278. https://doi.org/10.1016/j.biomaterials.2009.09.043.

[39] E. Soffer, J.P. Ouhayoun, A. Meunier, F. Anagnostou, Effects of autologous platelet lysates on ceramic particle resorption and new bone formation in critical size defects: the role of anatomical sites, J. Biomed. Mater. Res. B Appl. Biomater. 79 (2006) 86–94. https://doi.org/10.1002/jbm.b.30516.

[40] O. Bunk, M. Bech, T. Jensen, R. Feidenhans'l, T. Binderup, A. Menzel, F. Pfeiffer, Multimodal x-ray scatter imaging, New J Phys. 11 (2009). https://doi.org/10.1088/1367-2630/11/12/123016.

[41] M. Lebugle, M. Liebi, K. Wakonig, V.A. Guzenko, M. Holler, A. Menzel, M. Guizar-Sicairos, A. Diaz, C. David, High-acceptance versatile microfocus module based on elliptical Fresnel zone plates for small-angle X-ray scattering, Opt. Express. 25 (2017) 21145–21158. https://doi.org/10.1364/OE.25.021145.

[42] P. Kraft, A. Bergamaschi, Ch. Bronnimann, R. Dinapoli, E.F. Eikenberry, H. Graafsma, B. Henrich, I. Johnson, M. Kobas, A. Mozzanica, C.M. Schleputz, B. Schmitt, Characterization and Calibration of

PILATUS Detectors, IEEE Trans. Nucl. Sci. 56 (2009) 758–764. https://doi.org/10.1109/TNS.2008.2009448.

[43] M.H. Bünger, H. Oxlund, Y.K. Hansen, S. Sørensen, B.M. Bibby, J.S. Thomsen, B.L. Langdahl, F. Besenbacher, J.S. Pedersen, H. Birkedal, Strontium and bone nanostructure in normal and ovariectomized rats investigated by scanning small-angle X-ray scattering, Calcif. Tissue Int. 86 (2010) 294–306. https://doi.org/10.1007/s00223-010-9341-8.

[44] M.J. Turunen, S. Lages, A. Labrador, U. Olsson, M. Tägil, J.S. Jurvelin, H. Isaksson, Evaluation of composition and mineral structure of callus tissue in rat femoral fracture, J. Biomed. Opt. 19 (2014) 025003. https://doi.org/10.1117/1.JBO.19.2.025003.

[45] M. Doube, M.M. Kłosowski, I. Arganda-Carreras, F.P. Cordelières, R.P. Dougherty, J.S. Jackson, B. Schmid, J.R. Hutchinson, S.J. Shefelbine, BoneJ: Free and extensible bone image analysis in ImageJ, Bone. 47 (2010) 1076–1079. https://doi.org/10.1016/j.bone.2010.08.023.

[46] J. Schindelin, I. Arganda-Carreras, E. Frise, V. Kaynig, M. Longair, T. Pietzsch, S. Preibisch, C. Rueden, S. Saalfeld, B. Schmid, J.-Y. Tinevez, D.J. White, V. Hartenstein, K. Eliceiri, P. Tomancak, A. Cardona, Fiji: an open-source platform for biological-image analysis, Nat. Methods. 9 (2012) 676–682. https://doi.org/10.1038/nmeth.2019.

[47] N. Vordos, G. Drosos, I. Kazanidis, A. Ververidis, P. Ypsilantis, K. Kazakos, C. Simopoulos, A.C. Mitropoulos, S. Touloupidis, Hydroxyapatite Crystal Thickness and Buckling Phenomenon in Bone Nanostructure During Mechanical Tests, Ann. Biomed. Eng. 46 (2018) 627–639. https://doi.org/10.1007/s10439-018-1983-0.

[48] N. Mathavan, M.J. Turunen, M. Tägil, H. Isaksson, Characterising bone material composition and structure in the ovariectomized (OVX) rat model of osteoporosis, Calcif. Tissue Int. 97 (2015) 134–144. https://doi.org/10.1007/s00223-015-9991-7.

[49] J. Ballarre, I. Manjubala, W.H. Schreiner, J.C. Orellano, P. Fratzl, S. Ceré, Improving the osteointegration and bone–implant interface by incorporation of bioactive particles in sol–gel coatings of stainless steel implants, Acta Biomater. 6 (2010) 1601–1609. https://doi.org/10.1016/j.actbio.2009.10.015.

[50] C. Lange, C. Li, I. Manjubala, W. Wagermaier, J. Kühnisch, M. Kolanczyk, S. Mundlos, P. Knaus, P. Fratzl, Fetal and postnatal mouse bone tissue contains more calcium than is present in hydroxyapatite, J. Struct. Biol. 176 (2011) 159–167. https://doi.org/10.1016/j.jsb.2011.08.003.

[51] B. Zeller-Plumhoff, C. Malich, D. Krüger, G. Campbell, B. Wiese, S. Galli, A. Wennerberg, R. Willumeit-Römer, D.C.F. Wieland, Analysis of the bone ultrastructure around biodegradable Mg-xGd implants using small angle X-ray scattering and X-ray diffraction, Acta Biomater. 101 (2020) 637–645. https://doi.org/10.1016/j.actbio.2019.11.030.

[52] C. Burger, H. Zhou, H. Wang, I. Sics, B.S. Hsiao, B. Chu, L. Graham, M.J. Glimcher, Lateral Packing of Mineral Crystals in Bone Collagen Fibrils, Biophys. J. 95 (2008) 1985–1992. https://doi.org/10.1529/biophysj.107.128355.

[53] N. Claffey, H. Bashara, P. O'Reilly, I. Polyzois, Evaluation of New Bone Formation and Osseointegration Around Subperiosteal Titanium Implants with Histometry and Nanoindentation, Int. J. Oral Maxillofac. Implants. 30 (2015) 1004–1010. https://doi.org/10.11607/jomi.3647.

[54] T.B. Johnson, B. Siderits, S. Nye, Y.-H. Jeong, S.-H. Han, I.-C. Rhyu, J.-S. Han, T. Deguchi, F.M. Beck, D.-G. Kim, Effect of guided bone regeneration on bone quality surrounding dental implants, J. Biomech. 80 (2018) 166–170. https://doi.org/10.1016/j.jbiomech.2018.08.011.

[55] F.A. Shah, B. Nilson, R. Brånemark, P. Thomsen, A. Palmquist, The bone-implant interface – nanoscale analysis of clinically retrieved dental implants, Nanomedicine Nanotechnol. Biol. Med. 10 (2014) 1729–1737. https://doi.org/10.1016/j.nano.2014.05.015.

[56] E. Trofimov, R. Lutfullin, R. Kashaev, Elastic properties of the titanium alloy Ti-6Al-4V, Lett. Mater. 5 (2015) 67–69. https://doi.org/10.22226/2410-3535-2015-1-67-69.

[57] A. Anesi, M. Ferretti, F. Cavani, R. Salvatori, M. Bianchi, A. Russo, L. Chiarini, C. Palumbo, Structural and ultrastructural analyses of bone regeneration in rabbit cranial osteotomy: Piezosurgery versus traditional osteotomes, J. Cranio-Maxillo-Fac. Surg. Off. Publ. Eur. Assoc. Cranio-Maxillo-Fac. Surg. 46 (2018) 107–118. https://doi.org/10.1016/j.jcms.2017.10.004.

[58] A.A. Pesqueira, M.C. Goiato, H.G. Filho, D.R. Monteiro, D.M.D. Santos, M.F. Haddad, E.P. Pellizzer, Use of stress analysis methods to evaluate the biomechanics of oral rehabilitation with implants, J. Oral Implantol. 40 (2014) 217–228. https://doi.org/10.1563/AAID-JOI-D-11-00066.

[59] A. Kumar, R. Ghosh, R. Kumar, Effects of interfacial crack and implant material on mixed-mode stress intensity factor and prediction of interface failure of cemented acetabular cup, J. Biomed. Mater. Res. B Appl. Biomater. 108 (2020) 1844–1856. https://doi.org/10.1002/jbm.b.34526.

[60] M.C. Chang, C.C. Ko, C.C. Liu, W.H. Douglas, R. DeLong, W.-J. Seong, J. Hodges, K.-N. An, Elasticity of alveolar bone near dental implant–bone interfaces after one month's healing, J. Biomech. 36 (2003) 1209–1214. https://doi.org/10.1016/S0021-9290(03)00113-1.

[61] S. Ehrig, B. Schamberger, C.M. Bidan, A. West, C. Jacobi, K. Lam, P. Kollmannsberger, A. Petersen, P. Tomancak, K. Kommareddy, F.D. Fischer, P. Fratzl, J.W.C. Dunlop, Surface tension determines tissue shape and growth kinetics, Sci. Adv. 5 (2019) eaav9394. https://doi.org/10.1126/sciadv.aav9394.

[62] L. Pieuchot, J. Marteau, A. Guignandon, T. Dos Santos, I. Brigaud, P.-F. Chauvy, T. Cloatre, A. Ponche, T. Petithory, P. Rougerie, M. Vassaux, J.-L. Milan, N. Tusamda Wakhloo, A. Spangenberg, M. Bigerelle, K. Anselme, Curvotaxis directs cell migration through cell-scale curvature landscapes, Nat. Commun. 9 (2018) 3995. https://doi.org/10.1038/s41467-018-06494-6.

[63] J.E. Davies, Understanding peri-implant endosseous healing, J. Dent. Educ. 67 (2003) 932–949.

[64] C. Dahlin, J. Gottlow, A. Linde, S. Nyman, Healing of Maxillary and Mandibular Bone Defects Using a Membrane Technique: An Experimental Study in Monkeys, Scand. J. Plast. Reconstr. Surg. Hand Surg. 24 (1990) 13–19. https://doi.org/10.3109/02844319009004514.

[65] Z. Li, D. Betts, G. Kuhn, M. Schirmer, R. Müller, D. Ruffoni, Mechanical regulation of bone formation and resorption around implants in a mouse model of osteopenic bone, J. R. Soc. Interface. 16 (2019) 20180667. https://doi.org/10.1098/rsif.2018.0667.

8. Supplementary Data

Suppl 1 - Crystal thickness maps in the bone chambers (left) and the mature regions (right) for all specimens after 7 weeks (specimens S1 to S4) and 13 weeks of integration (specimens S5 to S8).